Shaping Effects on Non-Ideal Ballooning Mode*)

Haruki SETO, Masatoshi YAGI, Nobuyuki AIBA, Akinobu MATSUYAMA, Benjamin D. DUDSON[1)] and Xueqiao XU[2)]

National Institutes for Quantum and Radiological Science and Technology, Aomori 039-3912, Japan
[1)]*York Plasma Institute, Department of Physics, University of York, York YO10 5DD, UK*
[2)]*Lawrence Livermore National Laboratory, CA 94550, USA*

(Received 4 January 2018 / Accepted 4 June 2018)

The dependence of shaping effects on the growth rate of collisionless and resistive ballooning mode (CBM/RBM) is numerically investigated. That of the drift ballooning modes (DCBM/DRBM) is also investigated by taking kinetic effects into account. Resistivity scans of linear growth rates of CBM/RBM and DCBM/DRBM in a circular geometry show that both modes have 3 branches in accordance with decreasing resistivity, fast, resistive and collisionless branch. The last two branches are in the edge relevant resistivity regime and are in the scope of this paper. For CBM/RBM, shaping effect on the growth rate becomes weak with increasing resistivity and the growth rate monotonically increases with decrease of the elongation and increase of the triangularity, on the other hand, the opposite tendency appears on the triangularity for DCBM, namely it weakly decreases with increase of the triangularity. This fact indicates that the inverted D-shaped equilibrium can be unstable against DCBM compared with the D-shaped equilibrium.

Keywords: resistive ballooning mode, collisionless ballooning mode, plasma shaping, electron drift wave

DOI: 10.1585/pfr.13.3403086

1. Introduction

The H-mode discharge [1] is indispensable for fusion reactors from the viewpoint of the plasma confinement efficiency, while intermittent large heat fluxes released by edge localized modes (ELMs) [2] should be suppressed or mitigated for heat load constraints on plasma facing components. In the edge region of H-mode plasmas, collisionality changes drastically due to steep gradients of plasma temperature and density, which affects the edge plasma stability responsible for edge pedestal formation and ELM dynamics. It is therefore one of key issues to understand collisionality dependence of edge plasma instabilities.

For shaping effects on ballooning modes, a local theoretical analysis [3] predicted that the elongation $\kappa > 1$ can stabilize ballooning modes by weakening the poloidal curvature at the outer midplane. A local eigen value analysis on the resistive ballooning mode (RBM) [4, 5] in the collisional limit [6] also revealed that elongation $\kappa > 1$ and the negative triangularity $\delta < 0$ can stabilize and the positive triangularity $\delta > 0$ can destabilize ballooning modes.

In this paper, shaping effects of elongation and triangularity on collisionless ballooning mode (CBM) [7] and RBM in the presence of real electron inertia [8] are numerically investigated by BOUT++ code [9]. The remainder of this paper is organized as follows. In section 2, an equilibrium and a physics model are described. In section 3, shaping effects on CBM/RBM with and without electron drift wave and compression are numerically investigated. The summary is given in section 4.

2. Equilibrium and Physics Models

The axisymmetric toroidal expansion equilibrium [10] is employed to generate equilibria with different shaping factors having same normalized pressure gradient $\alpha(r) = -\epsilon q(r)^2 \beta'(r)$ and magnetic shear $s(r) = rq'(r)/q(r)$ profiles, where r is the minor radius, $\epsilon = r/R_{\rm ax}$ is the inverse aspect ratio, $R_{\rm ax}$ is the major radius at the magnetic axis, $q(r)$ is the safety factor, $\beta(r) = p(r)/(B_{\rm ax}^2/2\mu_0)$ is the pressure $p(r)$ normalized with the magnetic energy density at the magnetic axis, $B_{\rm ax}$ is the magnetic field intensity at the magnetic axis, μ_0 is the permittivity in vacuum and $'$ stands r-derivative respectively. In this model, the major radius R, the vertical position Z and the magnetic field $\mathbf{B}$ can be expressed with geometrical flux coordinates (r, χ, ζ),

$$R(r,\chi) = R_{\rm ax} - r\cos\chi - \Delta(r) - \sum_{m=2}^{\infty} S_m(r)\cos\left[(m-1)\chi\right], \quad (1)$$

$$Z(r,\chi) = r\sin\chi - \sum_{m=2}^{\infty} S_m(r)\sin\left[(m-1)\chi\right], \quad (2)$$

$$\mathbf{B}(r,\chi) = \nabla\zeta \times \nabla\psi + F\nabla\zeta, \quad (3)$$

$$F(r) = R_{\rm ax} B_{\rm ax}\left(1 + F_2(r)\right), \quad (4)$$

where χ is the geometrical poloidal angle, ζ is the geometrical toroidal angle, $\Delta(r)$ is the Shafranov shift, $S_m(r)$ is the

author's e-mail: seto.haruki@qst.go.jp

*) This article is based on the presentation at the 26th International Toki Conference (ITC26).

shaping factors providing m-th poloidal harmonic components of Grad-Shafranov equation (GSE), ψ is the poloidal flux function, $F(r)$ is the covariant toroidal field and $F_2(r)$ is the $O(\epsilon^2)$ correction of $F(r)/R_{\rm ax}B_{\rm ax}$ respectively.

Assuming the following ordering $\beta \sim r\beta' \sim F_2 \sim rF_2' \sim \Delta/R_{\rm ax} \sim \epsilon\Delta' \sim S_m/R_{\rm ax} \sim \epsilon S_m' \sim O(\epsilon^2)$, substituting Eqs. (1)-(4) into GSE and taking leading order terms of m-th harmonics of GSE, one obtains the ordinary differential equations (ODEs) for $F_2(r)$, $\Delta(r)$ and $S_m(r)$ shown in Appendix B of ref. [10]. These ODEs are solved with boundary conditions $F_2(0) = 0, \Delta(0) = \Delta'(0) = 0, S_m(a) = S_{ma}$ and holomorphic conditions of $S_m(0)$, where a is the minor radius at the last closed flux surface (LCFS) and S_{ma} is the m-th shaping coefficient at LCFS. It should be noted that contributions from pressure to $F_2(r)$ and $\Delta(r)$ are neglected for simplicity, which is valid in the low beta limit. In this paper, only $S_2(r)$ and $S_3(r)$ are taken, which are related with the Miller's elongation κ and triangularity δ [11],

$$S_{2a} \simeq a(1-\kappa)/(1+\kappa), \quad S_{3a} \simeq -a\delta/4, \tag{5}$$

where Eq. (5) is used as input parameters for S_2 and S_3.

BOUT++ code introduces orthogonal flux coordinates (ψ, θ, ζ) and field-aligned coordinates (x, y, z) [9, 12], where θ is the poloidal angle designed to make $\nabla\theta$ orthogonal to both $\nabla\psi$ and $\nabla\zeta$, x is the radial label, y is the parallel label based on θ and z is the binormal label respectively. It should be noted that the coordinate transformation between both flux coordinates can be expressed by,

$$r(\psi) = \int_0 \left[\frac{F(r)}{2\pi q(r)} \oint \frac{\mathcal{J}}{R^2} d\chi\right]^{-1} d\psi + a, \tag{6}$$

$$\chi(\psi,\theta) = \int_{r_0} \frac{g^{r\chi}}{g^{rr}} dr + \theta, \quad r_0 = r(\frac{\psi_{\rm in}+\psi_{\rm out}}{2}), \tag{7}$$

where $\mathcal{J}$ and g^{ij} are Jacobian and contravariant metric coefficients in the geometrical flux coordinates, $\psi_{\rm in} = \psi(r_{\rm in})$ is the poloidal flux function at the inner radial boundary $r = r_{\rm in}$, $\psi_{\rm out} = \psi(r_{\rm out})$ is that at the outer radial boundary $r = r_{\rm out}$ and the outer mid-plane (the bad-curvature plane) is given at $\theta = \pi$, (see Eqs. (1), (2) and (7)). Eq. (6) is obtained from the definition of $q(r)$ and Eq. (7) is also obtained from the orthogonal property of the orthogonal flux coordinates respectively.

Figure 1 shows examples of a series of equally-spaced grids for 1/50-th sector of tori having $\kappa = 1.0, 1.1, \cdots, 1.4$ and $\delta = -0.3, -0.2, \cdots, 0.3$ with $q(r) = 1 + 2(r/0.9a)^2$, $\beta(r) = \beta_0(1 - \tanh[50(r/a - 0.9)])/2$, $\beta_0 = 5 \times 10^{-4}$, $a = 0.5$ [m], $R_{\rm ax} = 2$ [m], $B_{\rm ax} = 2$ [T], $r_{\rm in}/a = 0.8$ and $r_{\rm out}/a = 1.0$ in common. These grids have resolutions with radial grid points $N_x = 1024, 2048, 4096$ for $0.8 \le r/a \le 1.0$, parallel grid points $N_y = 128$ for $0 \le y < 2\pi$ corresponding poloidal angle is shown in Fig. 1 (a) and binormal grid points $N_z = 128$ for $0 \le z < 2\pi/50$. These grids are fine enough compared with the electron skin depth $d_{\rm e} \sim 2 \times 10^{-3}$ [m] for the electron number density $n_{\rm e} = 10^{19}$[m^{-3}] even in the coarsest case with $N_x = 1024$

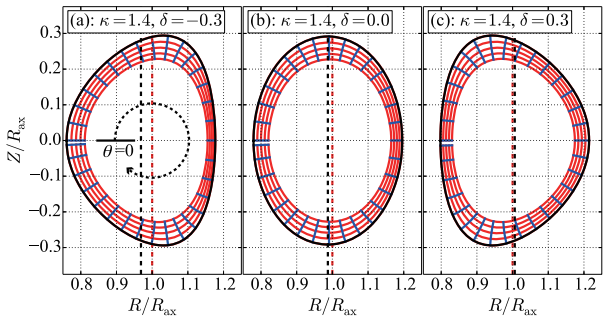

Fig. 1 Equilibria with same s and α profiles. (a): inverted D-shaped, (b): elliptic and (c): D-shaped equilibrium, where red dashed lines represent horizontal positions of the magnetic axis and black dashed lines represent those of the center of last closed flux surface (black solid). The relation between the poloidal angle θ and the geometry is also illustrated with the black dashed curve in figure (a).

for $\Delta x/B_{\rm p}R \sim \Delta r \sim 0.2a/N_x \sim 1 \times 10^{-4}$[m] $\ll d_{\rm e}$, where $B_{\rm p}$ is the poloidal magnetic field. The finer grids are employed to resolve fine radial structures appearing when CBM/RBM is coupled with the electron drift wave (DCBM/DRBM) in the low resistivity regime.

To investigate shaping effects on CBM/RBM, a fully linearized 4-field RMHD model [13] with Boussinesq and iso-thermal assumptions is employed. The 4-field model consists of vorticity equation, Ohm's law, energy equation and equation of ion parallel flow,

$$\frac{\partial}{\partial t}\nabla\cdot\left(\frac{\nabla_\perp\tilde{\phi}}{\bar{B}^2}\right) = -\bar{B}\nabla_\parallel\left(\frac{\nabla_\perp^2\tilde{A}_\parallel}{\bar{B}}\right) + \frac{\bar{\mathbf{b}}\times\bar{\boldsymbol{\kappa}}\cdot\nabla\tilde{p}}{\bar{B}}, \tag{8}$$

$$\frac{\partial}{\partial t}\left(\tilde{A}_\parallel - d_{\rm e}^2\nabla_\perp^2\tilde{A}_\parallel\right) = -\nabla_\parallel\tilde{\phi} + \eta\nabla_\perp^2\tilde{A}_\parallel + \delta_{\rm e}\left(\nabla_\parallel\tilde{p} - \frac{\bar{\mathbf{b}}\times\nabla_\perp\tilde{A}_\parallel\cdot\nabla_\perp\bar{p}}{\bar{B}}\right), \tag{9}$$

$$\frac{\partial\tilde{p}}{\partial t} = -\frac{\bar{\mathbf{b}}\times\nabla_\perp\tilde{\phi}\cdot\nabla_\perp\bar{p}}{\bar{B}} - \beta_*\left[\frac{2\bar{\mathbf{b}}\times\bar{\boldsymbol{\kappa}}\cdot\nabla\tilde{\phi}}{\bar{B}} + \nabla_\parallel\left(\frac{\tilde{v}_\parallel + 2\delta_{\rm e}\nabla_\perp^2\tilde{A}_\parallel}{\bar{B}}\right)\right], \tag{10}$$

$$\frac{\partial\tilde{v}_\parallel}{\partial t} = -\frac{1}{2}\left[\nabla_\parallel\tilde{p} - \frac{\bar{\mathbf{b}}\times\nabla_\perp\tilde{A}_\parallel\cdot\nabla_\perp\bar{p}}{\bar{B}}\right], \tag{11}$$

where ϕ is the electrostatic potential, B is the magnetic field intensity, $A_\parallel$ is the parallel magnetic potential, $\mathbf{b}$ is the unit vector along the field line, $\boldsymbol{\kappa}$ is the magnetic curvature, $d_{\rm e}$ is the electron skin depth, η is the resistivity, $\delta_{\rm e} = d_{\rm i}/4$ is the electron diamagnetic factor, $d_{\rm i}$ is the ion skin depth, $\beta_* = (5/3)\bar{p}/[1 + (5/3)\bar{p}/(2\bar{B}^2)]$ is the compressional factor, $v_\parallel$ is the ion parallel flow respectively.

Eqs. (8) - (11) assume the constant ion density n_0 and resistivity and are normalized by poloidal Alfvén units with $R_{\rm ax}$, $B_{\rm ax}$, $n_0 = 10^{19}$ [m^{-3}], $Z = 1$ and the deuterium mass. In addition, physical quantities are separated into equilibrium and perturbed parts as $f(x,y,z,t) = \bar{f}(x,y) + \tilde{f}(x,y,z,t)$ so that the equilibrium magnetic field

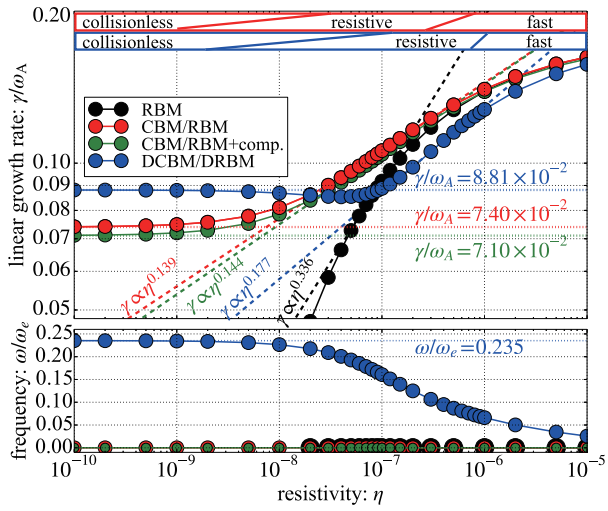

Fig. 2 $n = 50$ linear growth rate (top) and rotating frequency (bottom) versus resistivity in the circular geometry for RBM (black), CBM/RBM (red), CBM/RBM+comp. (green) and DCBM/DRBM (blue).

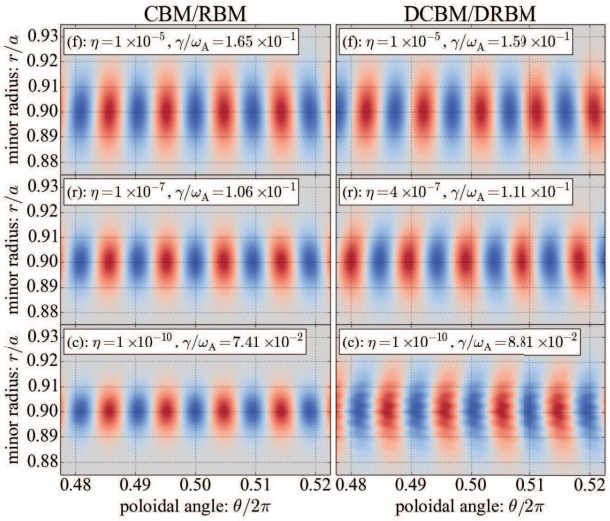

Fig. 3 Poloidal slices of pressure of CBM/RBM (left) and DCBM/DRBM (right) in (f): fast, (r): resistive and (c): collisionless branch around the outer mid-plane ($\theta/2\pi = 0.5$) in the circular geometry.

in Eq. (3) is redefined with the symbol $\bar{\mathbf{B}}$ and the perturbed magnetic field becomes $\tilde{\mathbf{B}} = \nabla\tilde{A}_\parallel \times \bar{\mathbf{b}}$.

Although the ion diamagnetic effect is neglected in the vorticity equation, the stabilization effect from two-fluid effects on ballooning modes is partially introduced via the electron Hall terms proportional to δ_e in Ohm's law.

3. Simulation Results

The following two models are employed to clarify shaping effects on CBM/RBM and DCBM/DRBM, Eqs. (8) - (11) with $d_e \neq 0, \delta_e = 0, \beta_* = 0$ for CBM/RBM and those with $d_e \neq 0, \delta_e \neq 0, \beta_* \neq 0$ for DCBM/DRBM.

Figure 2 summarizes resistivity dependence of linear growth rate and rotating frequency of $n = 50$ CBM/RBM and DCBM/DRBM in the circular geometry, where RBM described with $d_e = 0, \delta_e = 0, \beta_* = 0$ and CBM/RBM with compression (CBM/RBM+comp.) described with $d_e \neq 0$, $\delta_e = 0, \beta_* \neq 0$ are also tested as baselines for comparison. The reason why RBM growth rate deviates from $\gamma \propto \eta^{1/3}$ line in $\eta < 5\times10^{-7}$ is that radial intervals among rational q-surfaces compared with resistive skin depth become too wide to couple with poloidal sub-harmonics.

All modes show the fast ballooning nature [5] in the high resistivity regime $\eta \gtrsim 10^{-6}$. In this limit, instabilities are strongly localized in the parallel direction so that poloidal derivatives of eigen functions become comparable to radial derivatives of those. This fact means that local ballooning analyses are no longer valid, which results in a very weak dependence of linear growth rate on resistivity. It should be noted that the edge relevant resistivity regime lies roughly in $10^{-9} \lesssim \eta \lesssim 10^{-7}$ for $10^2 \lesssim T_e \lesssim 10^3$ [eV] so that shaping effects on ballooning modes in $\eta \lesssim 10^{-7}$ are in the scope of interest.

From comparison with RBM and CBM/RBM, the electron inertia has the significant impact on the growth rate in $\eta \lesssim 10^{-7}$ while it becomes less effective in the high resistivity regime. Comparison with CBM/RBM and CBM/CRBM+comp. also shows that CBM/RBM can be stabilized by coupling with compression of ion parallel flow and $E \times B$ flow.

One can find that the electron drift wave stabilizes ballooning modes in $\eta \gtrsim 10^{-8}$ while destabilizes them in $\eta \lesssim 10^{-8}$ by comparing growth rates of CBM/RBM+comp. with those of DCBM/DRBM. This result is consistent to a linear analysis on compressional effects including two-fluid effects on ideal ballooning mode [14]. The resistivity dependence of rotating frequency ω also shows that the plasma rotates in the electron diamagnetic direction $\omega > 0$ and goes to $\omega \simeq \omega_e/4$ in the collisionless limit $\eta = 0$ for DCBM/DRBM, while the plasma holds $\omega = 0$ for the other modes due to the absence of δ_e, where $\omega_e = -n\delta_e \frac{dp_0}{d\psi} = 0.409\omega_A$ is the electron diamagnetic frequency and $\omega_A = (B_{ax}/\sqrt{\mu_0 m_i n_0})/R_{ax} = 4.88\times10^6$ [Hz] is the poloidal Alfvén frequency respectively.

For classification of resistivity regimes, we introduce a resistive branch where the growth rate is proportional to the power law of resistivity and a collisionless branch where the growth rate goes to that in the collisionless limit as well as the fast branch corresponding to the too collisional limit. The resistivity regimes of each branch for CBM/RBM and DCBM/DRBM are shown in Fig. 2 with the red and the blue ribbon respectively, where oblique lines in these ribbons stand intermediate regimes for each mode.

Figure 3 shows poloidal slices of pressure $\tilde{p}(r, \theta, \zeta = 0)$ of CBM/RBM and DCBM/DRBM around the outer mid-plane $\theta = \pi$ in the circular geometry in fast, resistive and collisionless branch respectively. The eigen functions of CBM/RBM keep up-down symmetry given as initial perturbations in all branches, while those of

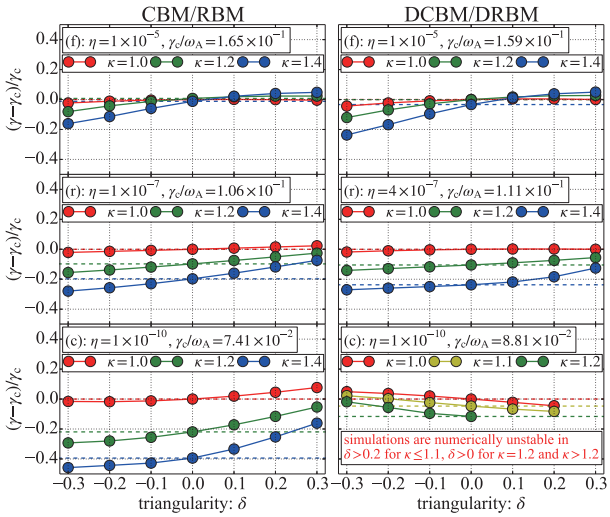

Fig. 4 Shaping effects on the linear growth rate of CBM/RBM (left) and DCBM/DRBM (right) in (f): fast, (r): resistive and (c): collisionless branch respectively, where γ_c is the growth rate in the circular geometry.

DCBM/DRBM rotate with finite frequencies so that up-down symmetry is not observed. The fine radial structure driven by the electron drift wave is observed in the collisionless branch for DCBM/DRBM.

Figure 4 summarizes shaping effects on the growth rate of CBM/RBM and DCBM/DRBM in the fast, the resistive and the collisionless branch respectively. For CBM/RBM, the elongation and the negative triangularity stabilize CBM/RBM by weakening the poloidal curvature $\kappa_p \approx (1/r)\mathbf{e}_r$ at the outer midplane while the positive triangularity destabilizes them by enlarging the poloidal curvature as reported in refs. [3, 6], where $\mathbf{e}_r$ is the unit vector in r-direction. This can be visually confirmed from the flux surfaces shown in Fig. 1. These tendencies never change in the edge relevant branches (or the resistive and the collisionless branch) but the impact of shaping effects however gets weaker with increasing resistivity so that realistic resistivity and electron mass are important in a quantitative manner. In the fast branch, the effect of elongation is negligibly small and that of triangularity gets large with elongation so that the elongation destabilizes RBM in the $\delta > 0$ cases, which only occurs in the unrealistically high resistivity regime and is out of the scope of this paper.

For DCBM/DRBM, the tendency of shaping effects in the resistive branch are same as that for CBM/RBM but the effect of triangularity gets inverted in the collisionless branch. It should be noted that simulations of DCBM/DRBM in the collisionless limit are numerically unstable in $\delta > 0.2$ for $\kappa \leq 1.1$, $\delta > 0$ for $\kappa = 1.2$ and $\kappa > 1.2$. Shaping effects on rotating frequencies of DCBM/DRBM also show different trends between the resistive and the collisionless branch as shown in Fig. 5. The electron drift wave, however, can either stabilize or destabilize DCBM/DRBM in this model, which is determined via a competition between the electron Hall terms and the compression of parallel current.

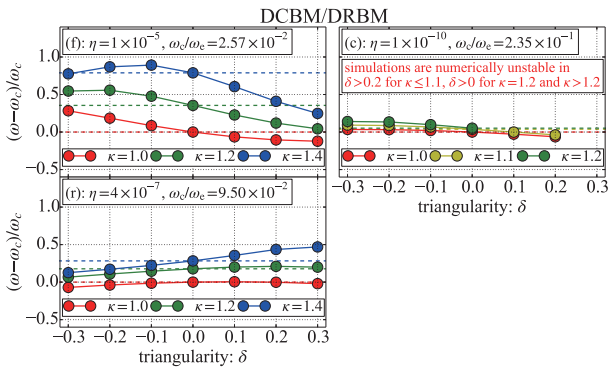

Fig. 5 Shaping effects on the rotating frequency in (f): fast, (r): resistive and (c): collisionless branch for DCBM/DRBM, where ω_c is the frequency in the circular geometry.

4. Summary

The dependence of shaping effects on growth rate of CBM/RBM and DCBM/DRBM has been numerically investigated. For CBM/RBM, shaping effect on the growth rate becomes weak with increasing resistivity and the growth rate monotonically increases with decrease of the elongation and increase of the triangularity, on the other hand, the opposite tendency appears on the triangularity for DCBM. These results have revealed that the electron drift wave can change the role of shaping effect of triangularity in the collisionless limit. This fact indicates that the inverted D-shaped equilibrium can be unstable against DCBM compared with the D-shaped one.

Acknowledgment

This work was partly supported by JSPS KAKENHI Grant No. 16K18342 and was also performed under the auspices of the U.S. Department of Energy by Lawrence Livermore National Laboratory under Contract No. DE-AC52-07NA27344. Computations were carried out on Selene at IFERC-CSC and on ICE-X at JAEA.

[1] F. Wagner *et al.*, Phys. Rev. Lett. **49**, 1408 (1982).
[2] H. Zohm, Plasma Phys. Control. Fusion **38**, 105 (1996).
[3] M. Yagi *et al.*, J. Phys. Soc. Jpn. **66**, 379 (1997).
[4] B.A. Carreras *et al.*, Phys. Rev. Lett. **50**, 503 (1983).
[5] L. Garcia *et al.*, Phys. Plasmas **6**, 107 (1999).
[6] F. Riva *et al.*, Plasma Phys. Control. Fusion **59**, 035001 (2017).
[7] F. Porcelli, Phys. Rev. Lett. **66**, 425 (1991).
[8] H. Seto *et al.*, Plasma Fusion Res. **11**, 1203122 (2016).
[9] B.D. Dudson *et al.*, Comput. Phys. Commun. **180**, 1467 (2008).
[10] J.P. Graves, Plasma Phys. Control. Fusion **55**, 074009 (2013).
[11] R.L. Miller *et al.*, Phys. Plasmas **5**, 973 (1998).
[12] M.A. Beer, Phys. Plasmas **2**, 2687 (1995).
[13] R.D. Hazeltine *et al.*, Phys. Fluids **28**, 2466 (1985).
[14] T. Rhee *et al.*, Phys. Plasmas **24**, 072504 (2017).